# Probabilistic Fretting Fatigue Assessment of Aircraft Engine Disks

**Michael P. Enright**

**Kwai S. Chan**
ASME Fellow

**Jonathan P. Moody**

Southwest Research Institute,
San Antonio, TX 78238

**Patrick J. Golden**
Air Force Research Laboratory,
Wright-Patterson AFB,
OH 45433

**Ramesh Chandra**

**Alan C. Pentz**

NAVAIR,
Patuxent River, MD 20670

*Fretting fatigue is a random process that continues to be a major source of damage associated with the failure of aircraft gas turbine engine components. Fretting fatigue is dominated by the fatigue crack growth phase and is strongly dependent on the magnitude of the stress values in the contact region. These stress values often have the most influence on small cracks where traditional long-crack fracture mechanics may not apply. A number of random variables can be used to model the uncertainty associated with the fatigue crack growth process. However, these variables can often be reduced to a few primary random variables related to the size and location of the initial crack, variability associated with applied stress and crack growth life models, and uncertainty in the quality and frequency of nondeterministic inspections. In this paper, an approach is presented for estimating the risk reduction associated with the nondestructive inspection of aircraft engine components subjected to fretting fatigue. Contact stress values in the blade attachment region are estimated using a fine mesh finite element model coupled with a singular integral equation solver and combined with bulk stress values to obtain the total stress gradient at the edge of contact. This stress gradient is applied to the crack growth life prediction of a mode I fretting fatigue crack. A probabilistic model of the fretting process is formulated and calibrated using failure data from an existing engine fleet. The resulting calibrated model is used to quantify the influence of inspection on the probability of fracture of an actual military engine disk under real life loading conditions. The results can be applied to quantitative risk predictions of gas turbine engine components subjected to fretting fatigue.* [DOI: 10.1115/1.4000130]

## 1 Introduction

The fatigue crack growth life of an aircraft gas turbine engine component is strongly dependent on the magnitude of the stress values that are applied during the lifetime of the component. It is well documented that component lifetimes can be significantly reduced when fretting fatigue occurs [1–5]. Fretting fatigue has been identified as one of the costliest sources of in-service damage related to high-cycle fatigue in the U.S. Air Force [6]. Component lifetimes can be reduced by as much as 40–60% or more depending on the severity of the loading [7,8]. Fretting occurs when two components are placed in contact and are subjected to cyclic loads that cause relative sliding and wear of the mating surfaces. If the magnitudes of the resulting displacements are relatively small (i.e., less than about 100 $\mu$m), partial slip occurs and the associated damage is classified as fretting [1,9].

Fatigue is often modeled as a two phase process consisting of (1) the formation or nucleation of an initial crack and (2) the crack propagation or growth. Over the past several decades, a number of approaches have been proposed to provide treatment for fretting fatigue based on one or both of these phases. Some researchers have focused on the adjustment of stress-life models [8,10,11], while others have developed models for the crack propagation phase [12–16]. However, a review of experimental observations suggests that fretting fatigue is dominated by the fatigue crack growth phase [17]. Furthermore, stress values in the contact region often have the most influence on small cracks where traditional long-crack fracture mechanics may not apply. Small-crack fretting models have recently emerged to address this issue [13,18,19].

The need for the application of probabilistic methods to fatigue life prediction is becoming increasingly recognized in the U.S. Over the past decade, the U.S. Federal Aviation Administration has released several advisory documents [20,21] that recommend the use of probabilistic methods for risk assessment of aircraft engine components. A number of probabilistic models have been developed to provide treatment of the crack nucleation and growth phases of fatigue. When the stress-life or strain-life approach is used to estimate life, random variables are often assigned to the regression coefficients associated with failure data [22,23]. A number of random variables can be used to model the uncertainty associated with the fatigue crack growth process. However, these variables can often be reduced to a few primary random variables related to the size and location of the initial crack, variability associated with applied stress and crack growth life models, and uncertainty in the quality and frequency of nondeterministic inspections [24].

In this paper, an approach is presented for estimating the risk reduction associated with the nondestructive inspection of aircraft engine components subjected to fretting fatigue. The approach is illustrated for an actual military engine disk under real life loading conditions. For aircraft engine disks, fretting typically occurs in the region where the blades are attached to the disk. Contact stress values in this region are estimated using a fine mesh finite element model coupled with a singular integral equation solver. These values are superimposed on the bulk stress values to obtain the total stress gradient at the edge of contact. This stress gradient is used to compute the local stress intensity factor range, the local stress ratio, and the corresponding crack propagation rate for a mode I fretting fatigue crack. Previous studies have shown that crack growth life estimates based on this approach are in agreement with values obtained from dovetail fretting fatigue specimens [25]. A probabilistic model of the fretting process is formulated and calibrated using available failure data from an existing engine

Contributed by the International Gas Turbine Institute (IGTI) of ASME for publication in the JOURNAL OF ENGINEERING FOR GAS TURBINES AND POWER. Manuscript received April 9, 2009; final manuscript received May 19, 2009; published online April 14, 2010. Editor: Dilip R. Ballal.


**Copyright © 2010 by ASME**

**Downloaded 02 Jun 2010 to 171.66.16.96. Redistribution subject to ASME license or copyright; see http://www.asme.org/terms/Terms_Use.cfm**

fleet. The resulting calibrated model is used to quantify the influence of inspection on the probability of fracture of military engine disks subjected to fretting fatigue.

## 2 Fretting Stress Modeling

A finite element method (FEM) analysis of a blade and disk assembly can be used to obtain either the contact loads or stresses required for a probabilistic assessment. This alone can be a difficult task due to the nonlinear contact analysis required and complex geometry of the components. Prior work by Calcaterra and Naboulsi [26] was performed to investigate contact damage in aircraft engine hardware. They analyzed two blade and disk attachments from the same compressor stage of two similar engines operated by the U.S. Air Force. They concluded that a FEM analysis was not sufficient to predict the contact stresses at the edge of contact. Instead, they implemented a hybrid process in which both the FEM and the singular integral equation (SIE) solution tool CAPRI were applied. Comparisons of the components were made based on the Smith–Watson–Topper approach for computing the crack initiation life, but the authors were unable to correlate the observed fretting fatigue life with the local contact stress calculation. That work did not explore the use of fracture mechanics to predict damage growth in the contact stress field. Golden and Calcaterra [25] showed that fracture mechanics methods using the contact stress analysis were able to predict the lives of dovetail fretting fatigue specimens. That analysis, however, was not applied to real components, and was confined to constant amplitude loading. Mission loading, particularly in a dovetail attachment, can become quite complicated. Gean and Farris [27] demonstrated a method to predict contact forces for a prescribed engine speed and thermal mission. This type of methodology is essential for improving the efficiency and accuracy of FEM component contact analyses for complex missions.

The normal contact force per unit thickness $P$ associated with fretting can be obtained by integration of the pressure $p$ in the contact region over the contact length $x$

$$P = \int p(x)dx \tag{1}$$

Prior work has shown that contact forces can be accurately predicted even with fairly coarse meshes [28]. Likewise, the shear traction $q$ can be integrated over the contact length to obtain the shear contact force per unit thickness $Q$

$$Q = \int q(x)dx \tag{2}$$

The contact moment per unit thickness $M$ about the center of contact is equal to the integral of the product of the contact pressure $p$ and the distance from the center of contact $x_0$

$$M = \int (x - x_0)p(x)dx \tag{3}$$

The relationship among contact forces $P$ and $Q$ is illustrated in Fig. 1 for a typical fan speed profile. In Fig. 1, the dashed lines indicate the bounds imposed by the coefficient of friction $\mu$. When $Q = \mu P$, the contact is called "sliding" or "gross slip." When $|Q| < \mu P$ the contact is referred to as "partial slip." The slope $\alpha$ of the $Q$ versus $P$ curve during partial slip is a characteristic of the component. This slope is used to predict more complex histories of $Q$ and $P$ as described later in the paper.

Contact stresses can be obtained directly from the contact forces and moments using the numerical solution of the SIEs that characterizes the contact interface using the CAPRI software [29] or the worst case fret (WCF) model [30]. The CAPRI SIE solver was developed to calculate contact stresses for a random shaped indenter pressing into a flat plate with a shear force applied using a Fourier transform technique [29].

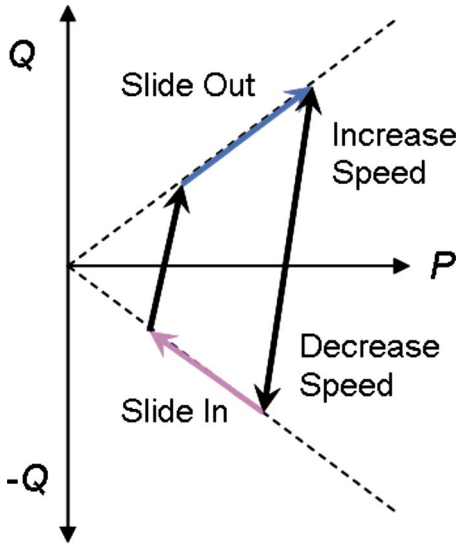


**Fig. 1 Illustration of the relationship among contact forces *P* and *Q* in the disk/blade interface of a typical gas turbine engine**

The WCF model [30] was developed to treat the propagation and arrest of small cracks under the influence of the fretting stress field in the presence of a remotely applied bulk stress. The WCF model considers a flat pad with round edges of radius $r$ fretting on a half plane. The flat pad is subjected to a normal load $P$ and a shear force $Q$. A bulk stress $S$ is applied in the half plane. The contact stress field for the flat pad can be obtained for a given set of $P$ and $Q$ values.

The distributions of normal traction $p(x)$ and shear traction $q(x)$ on the fretting surfaces are first computed using the singular-integral-equation formulation by Ciavarella et al. [31]. Series expansions are then performed for $p(x)$ and $q(x)$ in terms of Chebyshev's polynomials, which are then utilized to obtain the Mushkelishivili potential. Subsequently, the interior stress field is evaluated from Mushkelishivili's potential using standard equations and the results are added to the bulk stress to provide the total fretting fatigue stresses. The fretting stresses are then utilized to compute the stress intensity factors and fatigue crack growth rate response. Details of the governing equations and the computational procedures were reported in an earlier paper [30].

## 3 Uncertainty Modeling

When failure data are available, the probability of fretting failure can be estimated from a direct fit of the data. However, to quantify the influence of inspection, a physics-based probabilistic model is required to estimate the random sizes of propagating cracks. The probabilistic model can be calibrated to match the component failure data, and can be used to quantify the influence of inspection on the probability of fracture.

For example, consider an aircraft fleet in which premature cracks are found in some but not all of the engines. The measured crack area can be plotted versus cycles, as illustrated in Fig. 2. The observed probability of cracking $P_c$ is based on the number of engines with premature cracks $N_c$ and the total number of engines in the fleet $N_t$

$$P_c = \frac{N_c}{N_t} \tag{4}$$

$P_c$ can be predicted using a physics-based probabilistic model, where the predicted probability of cracking is given by



Downloaded 02 Jun 2010 to 171.66.16.96. Redistribution subject to ASME license or copyright; see http://www.asme.org/terms/Terms_Use.cfm

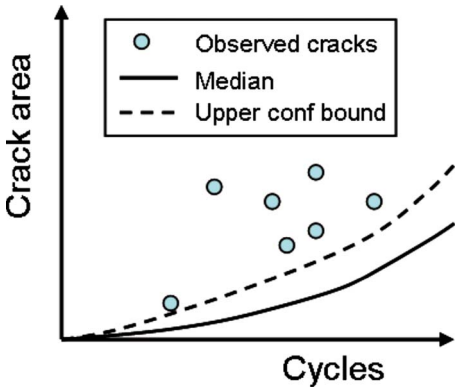


**Fig. 2 For the probabilistic calibration, the upper confidence bound of predicted crack area is set equal to the smallest observed crack area**

$$P_c = P(a > a^*) \tag{5}$$

This is shown conceptually in Fig. 3, where $P_c$ is the area under the crack area probability density function (PDF) to the right of $a^*$ (i.e., shaded region). $a^*$ is the smallest observed crack area, and can be considered as an upper confidence bound value above which the probability of crack occurrence is given by $P_c$. To calibrate the probabilistic model, the predicted crack area PDF is adjusted so that the predicted $P_c$ matches the observed $P_c$ for a specified value of $a^*$.

A number of variables can be included in the probabilistic computations to model the uncertainty [24]. However, for the calibration process, it is assumed that the difference between the predicted and measured values is due to variability in the applied stress values. A stress scatter random variable is introduced that is applied to the nominal values associated with bulk and fretting stresses. The median value of this factor is set to 1.0, and the coefficient of variation is adjusted so that the area under the crack area PDF to the right of $a^*$ matches the observed $P_c$. Note that this model does not account for the variability in the observed $P_c$.

## 4 Application to Military Aircraft Gas Turbine Engine Disk

The probabilistic methodology was applied to an actual military engine disk under real life loading conditions. A finite element analysis was performed to obtain the contact forces, which were converted to stress values and applied to assess the risk of fracture and risk reduction associated with inspection.

**4.1 Finite Element Analysis.** A finite element method analysis of the disk-blade assembly was carried out to obtain contact forces and moments along the disk-blade interface associated with applied inertial and static aerodynamics forces on the airfoil. Due to the complex geometry of the fan blade, quadratic tetrahedral elements were used for the associated finite element mesh. A refined mesh of first order hexahedral elements was used for the dovetail portion of the fan blade and the disk [28]. This element type was selected for its superior performance in the contact interface.

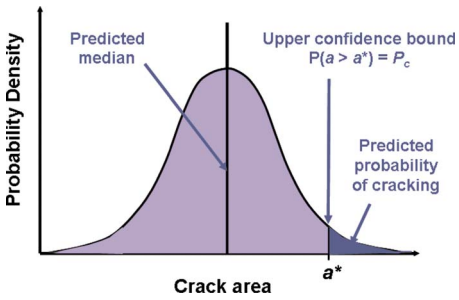


**Fig. 3 The probabilistic model is calibrated to the failure data by adjusting the predicted probability of cracking to match the occurrence rate observed in the actual disk population**

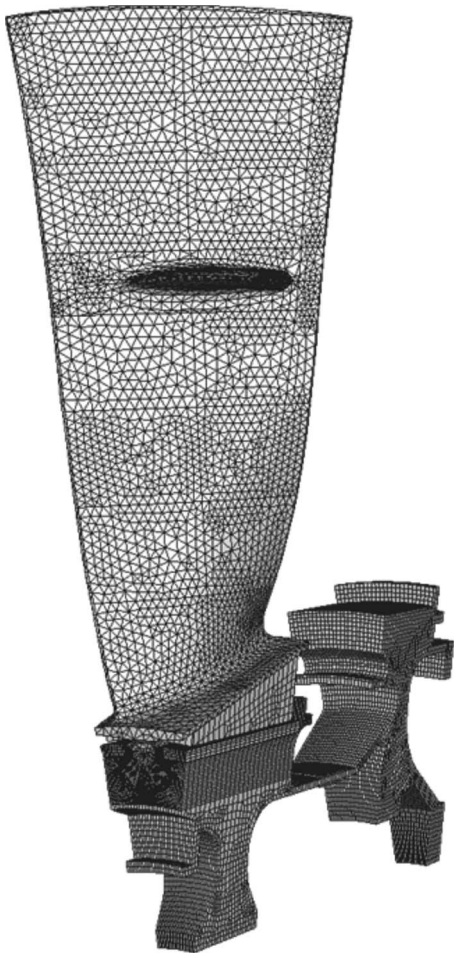

**Fig. 4 Due to the complex geometry of the fan blade, higher order tetrahedral elements (C3D10) were used for the associated finite element mesh**

The final mesh for the disk-blade assembly and for the interface region between the dovetail portion of the blade and the disk is shown in Figs. 4 and 5, respectively. The dovetail is aligned along the axial direction of the engine. A single blade and section of the disk were modeled using cyclic symmetry to represent the entire rotor. The entire mesh had approximately 121,000 elements including 800 elements in contact on the disk side of the interface and approximately 400 elements on the dovetail side of the interface. The model was solved using the ABAQUS software using a surface-to-surface contact formulation [32] with a coefficient of friction among surfaces set to a value of 0.7. Load cases available for analysis included 50%, 72%, and 110% maximum fan speed. A simple mission (0%, 110%, 50%, 110%, and 72%) was built for the FEM analysis that would allow contact force history effects to be analyzed. Convergence of the nonlinear analysis required that each load step in the mission be broken into 15–25 increments resulting in a total of 87 increments available for postprocessing. Computation time was approximately 24 hours using four processors.

Results from the FEM analysis indicated that the contact pressure and shear tractions varied considerably along the length of the dovetail slot. The highest contact pressure occurred at the



Downloaded 02 Jun 2010 to 171.66.16.96. Redistribution subject to ASME license or copyright; see http://www.asme.org/terms/Terms_Use.cfm

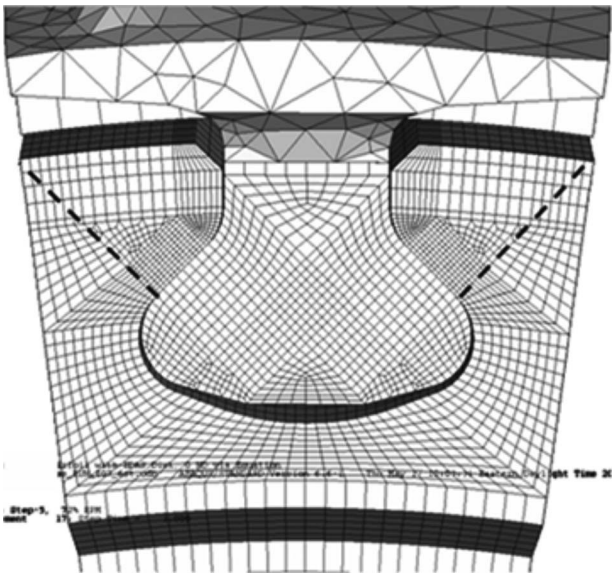

**Fig. 5 A refined mesh of first order hexahedral elements (C3D8) was used for the dovetail portion of the fan blade and the disk**

forward edge of the high pressure side of the dovetail interface and at the aft edge of the low pressure side of the dovetail interface. The high aerodynamic pressure and low aerodynamic pressure sides were defined by the aerodynamic forces on the airfoil. To quantify the variation in contact forces along the length of the dovetail slot, the model was "sliced" into 12 sections that could then be further analyzed independently. The slices, shown in Fig. 6, were equally spaced and numbered 1 through 12 with number 1 nearest the forward edge of the disk. Each slice represented two columns of brick elements and an axial depth of about 9 mm.

Contact pressure and shear tractions were extracted from each of the 24 total slices (12 each on the high pressure and low pressure sides) at each increment of load. An example of the pressure $p$ and shear $q$ tractions for one slice and at one load increment is shown in Fig. 7. The coordinate $x$ is along the surface of the interface and is perpendicular to the axial direction of the slot. The geometry of the contacting surfaces along the $x$ direction was flat with rounded edges. This resulted in the contact tractions, as shown, where the peak pressure and shear occurred near the edges

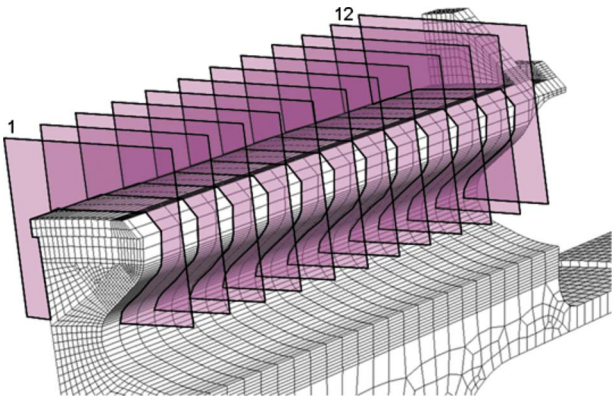


**Fig. 6 To quantify the variation in contact forces along the length of the dovetail slot, the finite element model was sliced into 12 sections that could then be further analyzed independently**

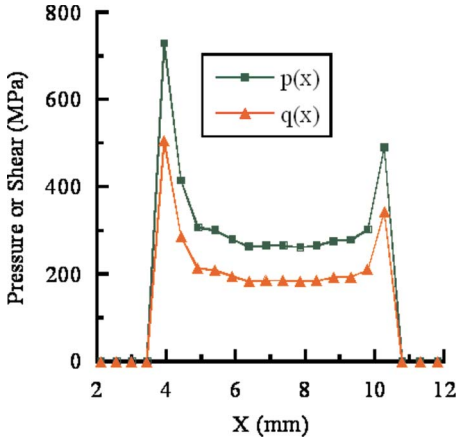


**Fig. 7 Pressure and shear tractions from finite element model results for slice number 1 and load increment 1**

of contact. Note that the results are fairly coarse due to the limited number of contact elements.

Contact forces for the individual slices were identified using Eqs. (1)–(3). Note that the units for the contact forces are force per unit thickness and moment per unit of thickness where thickness was the material included in each slice. The $Q$ versus $P$ history for slice number 1 is shown in Fig. 8.

The FEM analysis results were also used to estimate the bulk stress values. The bulk stress is defined as the stress in the component in the absence of the local contact stresses. The analytical tools described later in this paper have the capability to accurately predict the contact stress. However, they cannot predict the entire stress gradient because they do not include all of the component geometry and loading information.

To obtain the bulk stress values, the multi-axial components of stress were extracted from the FEM results along a path perpendicular to the contact interface starting at the edge of contact. This path is shown in Fig. 5 as a dashed line on both the high pressure and low pressure sides of the dovetail slot.

Stress values were extracted from the FEM results for each slice and load increment. An example is shown in Fig. 9, in which $x$ is parallel to the contact surface in the plane of the slice, $y$ is in the direction of the path, and $z$ is out of the plane in the axial direction of the slot. As expected, the crack opening stress $\sigma_{xx}$ was clearly the dominant component of stress (although it included some influence from the contact interface). This stress gradient could not simply be used as the contact stress because it was not converged. Instead, the near surface portion was ignored and the

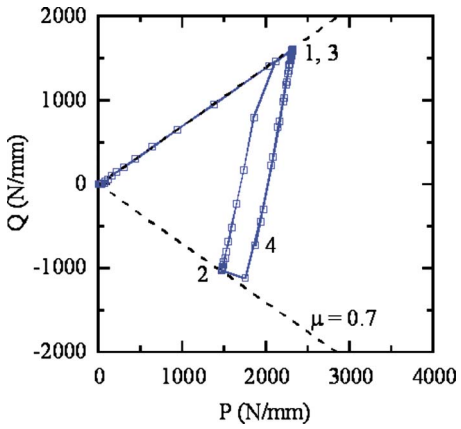


**Fig. 8 Contact force history for one slice of the finite element model: 1. 110% maximum speed, 2. 50%, 3. 110%, and 4. 72%**



Downloaded 02 Jun 2010 to 171.66.16.96. Redistribution subject to ASME license or copyright; see http://www.asme.org/terms/Terms_Use.cfm

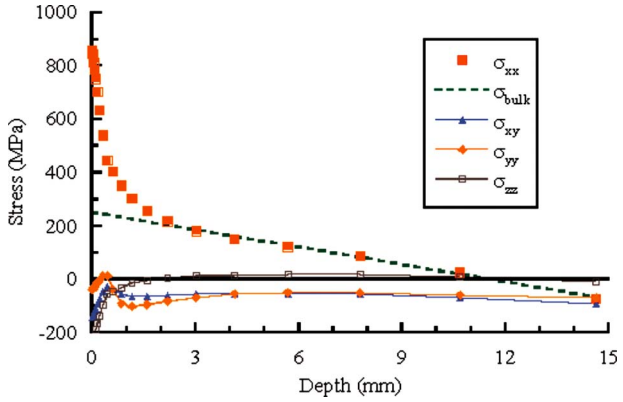


**Fig. 9 Bulk stresses were obtained from the finite element model along a path perpendicular to the edge of contact for a single slice and load increment**

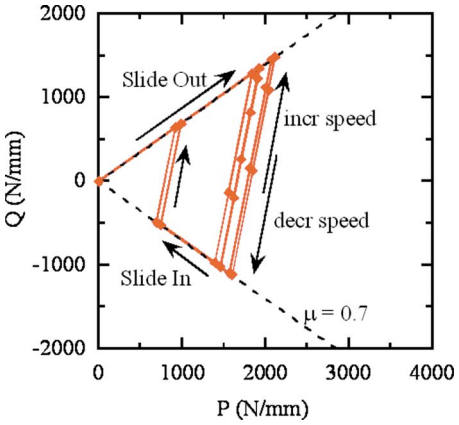


**Fig. 11 Representative *P* and *Q* history for the typical fan speed profile shown in Fig. 10**

remainder was linearly fit and extrapolated back to the surface to obtain $\sigma_{bulk}$. The other multi-axial components of stress were not included in this analysis since they were relatively small.

The simplified mission profile described earlier (0%, 110%, 50%, 110%, and 72%) was used for the finite element analysis for two reasons: (1) to limit the computational time needed for the analysis and (2) because the aerodynamic loads were only available at those speeds. The actual mission for the component of interest was more complex than the one used in the FEM analysis. It was represented using the composite mission shown in Fig. 10, which consists of 32 speed reversals and includes both major and minor reversals.

A method was needed to predict the contact forces and bulk stress for this mission given the results of the FEM analysis, such as the method developed by Gean and Farris [27]. In general, the predictions could incorporate changes in both speed and temperature. However, the disk was assumed to be under isothermal conditions, so stress values associated only with speed changes were considered. The moment remained small and constant with speed for all of the dovetail slot slices considered. Also, it was found that the bulk stress was nearly proportional to the square of the speed, so the discussion will be limited to $P$ and $Q$.

Several constraints were applied to predict the $P$ and $Q$ history given the speed history and are included as Eqs. (6)–(8). $P$ and $Q$ are subscripted with the index $i$ since the equations applied to each slice. As indicated in Eq. (6), the sum of the radial components of $P$ and $Q$ times their slice thickness $t$ must equal the total radial force applied by the blade. This blade force is proportional to the square of the rotor speed $\Omega$

$$F_{\text{blade}} = \sum [t_i \cdot (P_i \cos\theta + Q_i \sin\theta)] \propto \Omega^2 \tag{6}$$

An example prediction of $Q$ versus $P$ is shown in Fig. 11 for the mission shown in Fig. 10. Initially, the blade "slides out" in the slot due to the frictional shear force exceeding that required for slip and following the dashed line defined by

$$|Q_i| \leq \mu P_i \tag{7}$$

Next, the speed decreases but the blade remains wedged or stuck in place and the $Q$ versus $P$ path follows the slope $\alpha$ down as described by Eq. (8)

$$\Delta Q_i = \alpha_i \Delta P_i \tag{8}$$

If the speed decreases enough, however, the blade will become unstuck and "slide in," which is shown by the lower dashed line in Fig. 11. When speed increases again, $P$ and $Q$ move up along slope $\alpha$ until the upper dashed line is reached then the blade again slides out.

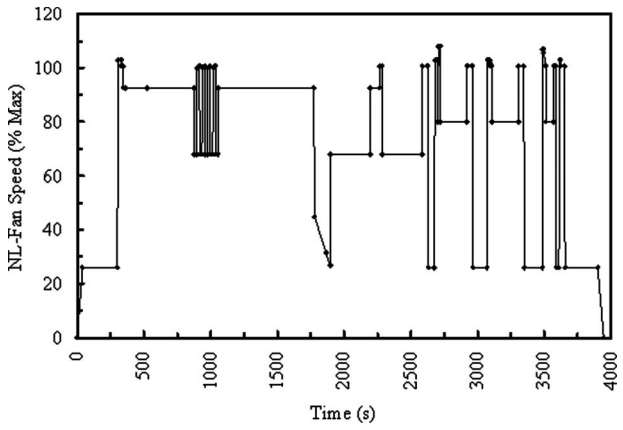


**Fig. 10 Typical fan speed profile based on the composite mission associated with actual engine usage histories**

**4.2 Contact Stresses.** The CAPRI [29] and WCF [30] models were utilized to compute the contact stresses associated with a blade fretting on a disk. The input parameters to both models included Young's modulus ($E$=107 GPa), Poisson's ratio ($\nu$=0.33), coefficient of friction ($\mu$=0.7), pad radius (4.955 mm), and the length of the flat pad (6.466 mm). The normal ($P$) and tangential ($Q$) forces on the contact surfaces as well as the bulk stresses ($S$) in the disk were obtained from the finite element analyses of the blade/disk assembly.

The pressure and tangential loads for individual steps of a mission as given by FEM analyses were utilized to compute the contact stresses at the trailing edge of contact for various depths beneath the contact surface. The contact stresses were then summed with the bulk stress to obtain the total stress profile along a specified direction. For illustration, the computed total stress profiles for the first slice on the high pressure side (Hi01) at load step 1 and step 2 of the mission are presented in Fig. 12. Load step 1 resulted in a tensile stress at the trailing edge of contact because of a positive (clockwise) shear force, while step 2 resulted in a compressive stress due to a negative (counterclockwise) shear force. In the WCF computations, the moments acting on the blade were ignored, whereas the CAPRI computations included the moments. For both load steps, the total stresses computed by CAPRI and WCF were essentially identical except near the edge of contact on the surface ($y$=0), as shown in Fig. 12. The WCF formulation predicted slightly higher stresses near the edge of contact surface



Downloaded 02 Jun 2010 to 171.66.16.96. Redistribution subject to ASME license or copyright; see http://www.asme.org/terms/Terms_Use.cfm

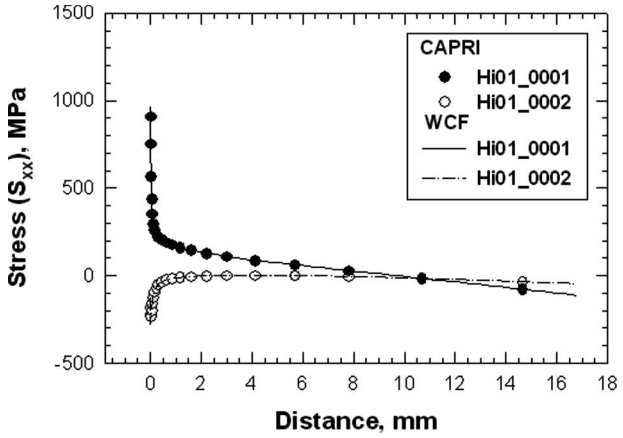


**Fig. 12 Computed total stress values for high pressure slice 1 at mission load steps 1 and 2**

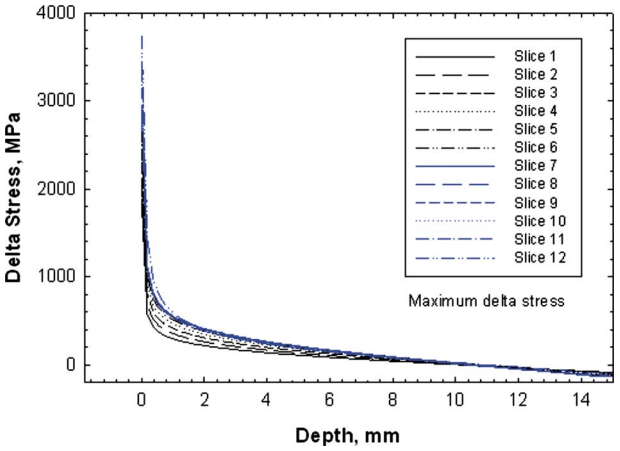


**Fig. 14 Maximum delta stress values for high pressure slices**

at a distance less than 5 $\mu$m from the surface. This was probably due in part to ignoring the contact moment. At a crack depth of about 1.5 mm, the contact stress diminished to very low values and the total stress equaled the bulk stress. Figure 13 is a comparison of the total stresses at steps 1 and 2 and at slices 1, 6, and 12. This plot shows that the total stresses were slightly higher toward the center slices of the dovetail slot, mostly due to a higher bulk stress. Maximum delta stress values for all slices are shown in Fig. 14.

The stress ranges associated with load steps 1 and 2 are shown as a function of distance from the contact surface in Fig. 15, which also shows the bulk stress range and the threshold stress range for a large-crack fatigue crack growth threshold of 2 MPa(m)$^{1/2}$. The bulk stress range is less than the threshold stress for crack growth when the crack depth is less than 200 $\mu$m. Thus, a microcrack less than 200 $\mu$m in depth would not grow if the bulk stress acted alone. In contrast, the total stress ranges computed by CAPRI and WCF, which were in agreement, were higher than the threshold stress range and a microcrack could propagate as a large crack.

**4.3 Fracture Risk Assessment.** Information regarding a number of random variables is typically required to perform a probabilistic fracture assessment. These variables can be categorized into six primary groups related to the size and location of the initial crack, variability associated with applied stress values and crack growth life models, and uncertainty in the frequency and quality of the nondestructive inspection [33]. For this example, data were not available to characterize these variables. However, previous depot inspections revealed premature cracking in some disks, shown in Fig. 16.

Using total stress values from the FEM results, crack area versus flight hour values were computed for each of the 12 slices using the DARWIN® probabilistic fracture mechanics software [33].

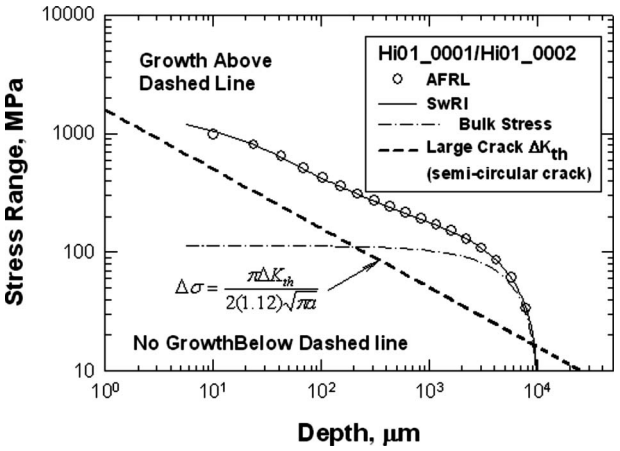


**Fig. 15 Computed stress ranges for high pressure slice 1 corresponding to load steps 1 and 2 compared with the bulk stress range and the threshold stress ranges for a large-crack growth threshold $\Delta K_{th}$ of 2 MPa(m)$^{1/2}$**

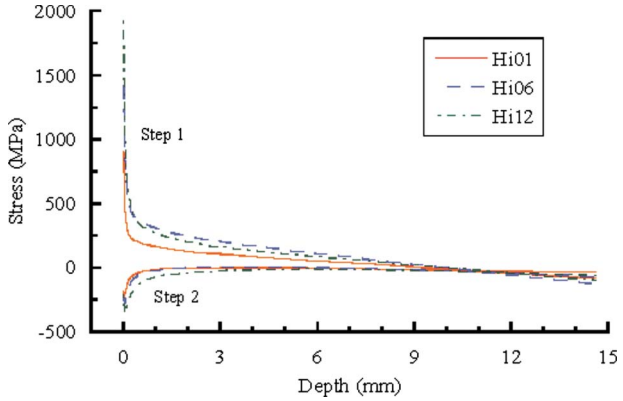


**Fig. 13 Computed total stress values for high pressure slices 1, 6, and 12 at mission load steps 1 and 2**

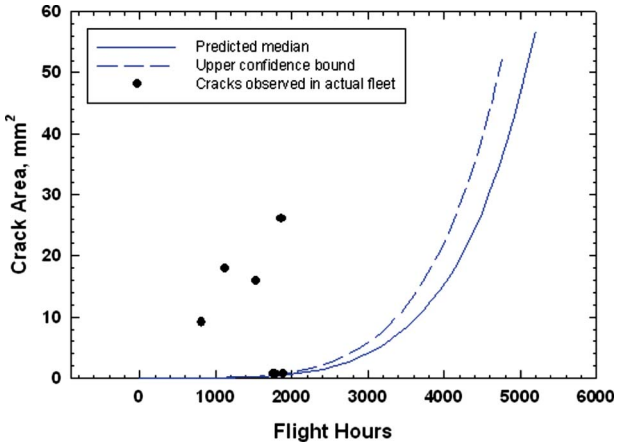


**Fig. 16 The stress scatter coefficient of variation (COV) was adjusted so that the upper confidence bound was equal to the smallest observed crack size**



Downloaded 02 Jun 2010 to 171.66.16.96. Redistribution subject to ASME license or copyright; see http://www.asme.org/terms/Terms_Use.cfm

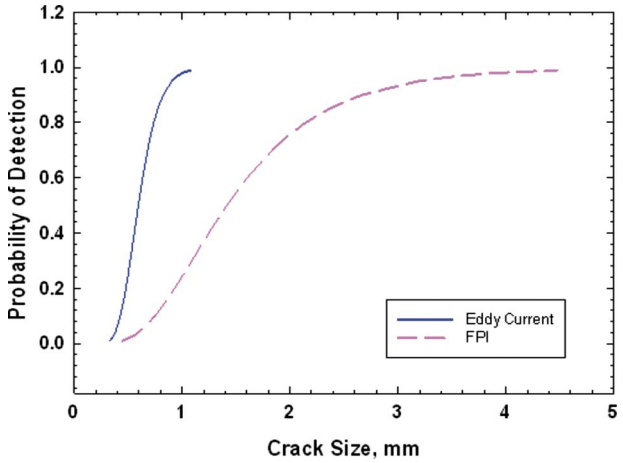


**Fig. 17 POD plots for representative eddy current and FPI inspection methods**

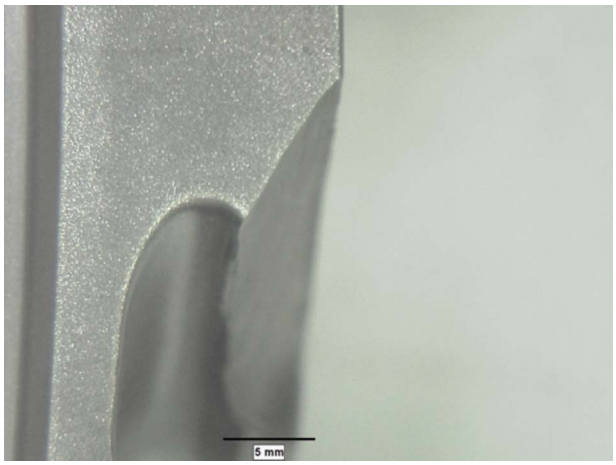


**Fig. 20 The crack propagation plane associated with fretting fatigue often is not perpendicular to the surface of contact**

The median value of crack area versus hours for the 12 slices is shown in Fig. 16. The stress variability was adjusted so that the predicted $P_c$ matched the observed $P_c$. As shown in Fig. 16, the crack growth life associated with the upper bound stress value passes through the smallest observed crack, as expected.

The primary objective of this study was to quantify the influence of inspection on the probability of fracture of military engine disks subjected to fretting fatigue. Two nondestructive inspection techniques were considered: eddy current (EC) and fluorescent penetrant inspection (FPI). The probability of detection (POD) curves for the selected inspection methods are shown in Fig. 17. Fracture risk computations were performed using DARWIN [33]. Normalized probability of fracture results are shown in Figs. 18 and 19 for the EC and FPI techniques, respectively. From Figs. 18 and 19 it can be concluded that the risk reduction associated with the two inspection techniques are nearly identical, and that the overall risk reduction is strongly dependent on the inspection interval.

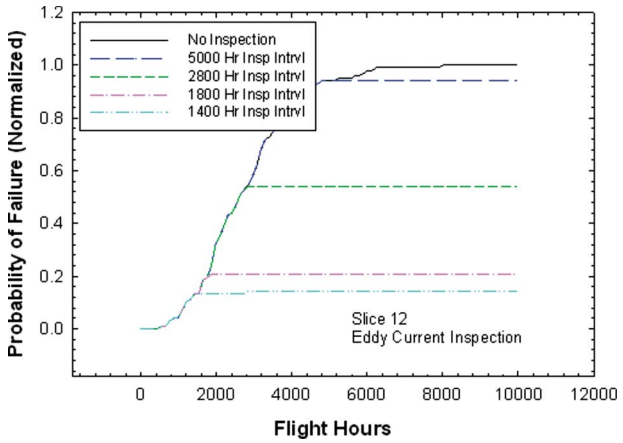


**Fig. 18 Influence of eddy current inspection on the normalized probability of fracture for selected inspection intervals**

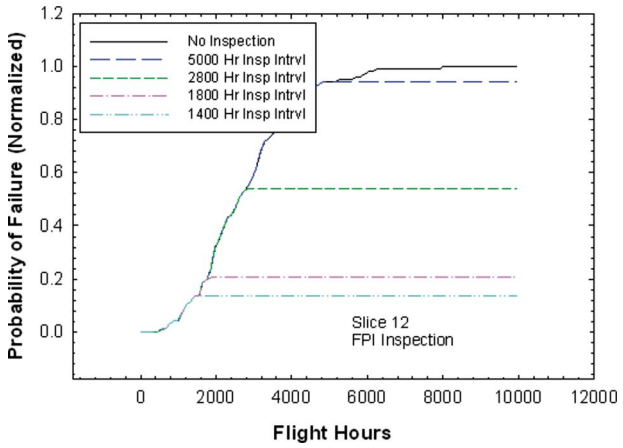


**Fig. 19 Influence of FPI inspection on the normalized probability of fracture for selected inspection intervals**

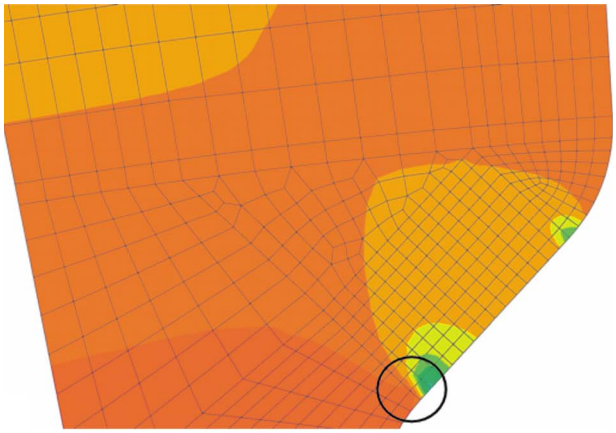

(*a*)

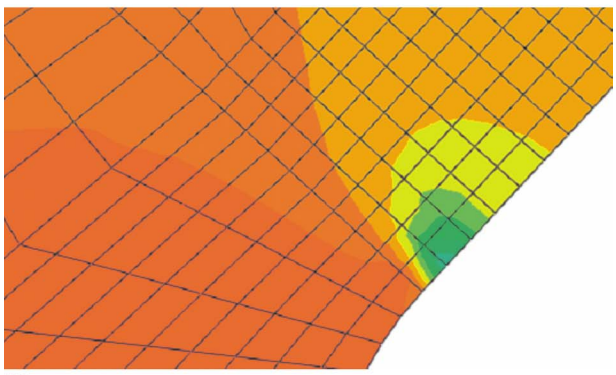

(*b*)

**Fig. 21 Principal stress values associated with a representative load step: (*a*) maximum principal stress contours and (*b*) enlarged view at the edge of contact**



Downloaded 02 Jun 2010 to 171.66.16.96. Redistribution subject to ASME license or copyright; see http://www.asme.org/terms/Terms_Use.cfm

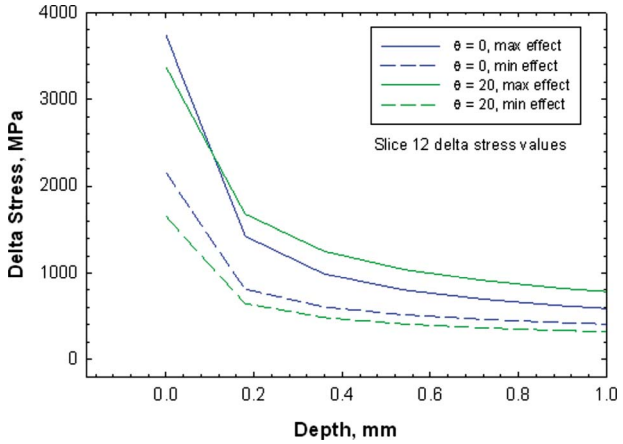


**Fig. 22 Influence of crack path orientation on slice 12 delta stress gradient**

## 5 Influence of Crack Path on Fracture Risk

When a component is subjected to fretting, microcracks can form on a plane that is perpendicular to the contact surface. However, in failed specimens (e.g., Fig. 20), the resulting crack propagation plane is not perpendicular to the surface. Principal stress values in the contact region are shown in Fig. 21 for a representative slice and load step of the disk-blade model shown in Figs. 4 and 5. An enlarged view of the edge of contact (Fig. 21(*b*)) reveals that the largest principal stress values do not occur on a path that is perpendicular to the contact surface, but roughly 20 deg from the perpendicular path.

Stress gradients associated with the two crack paths are shown in Fig. 22 for minimum and maximum delta stress values for a representative slice. It can be observed that, except within about 100 $\mu$m from the surface, the maximum delta stress values associated with the 20 deg crack path exceed those of the 0 deg (i.e., perpendicular) crack path. As shown in Fig. 23, the fracture risk values associated with the 20 deg crack path are larger than those for the 0 deg path, as expected.

The crack propagation shape is dominated by the steep fretting stress gradient at the surface. As shown in Fig. 24(*a*), the predicted crack advances more quickly on the contact surface compared with the adjacent surfaces. This behavior is observed in failed specimens, such as the one shown in Fig. 24(*b*).

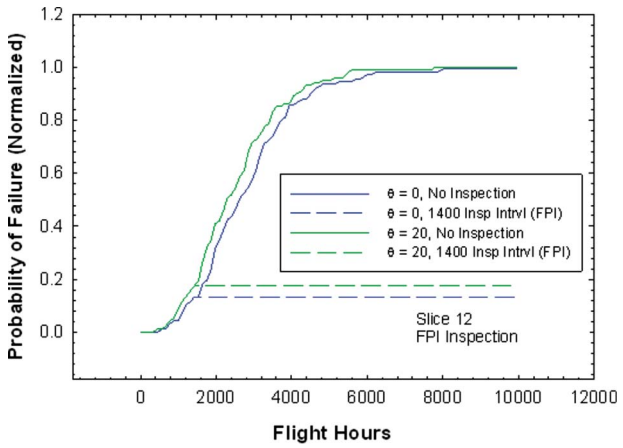


**Fig. 23 Influence of crack path orientation on the normalized probability of fracture of selected slices**

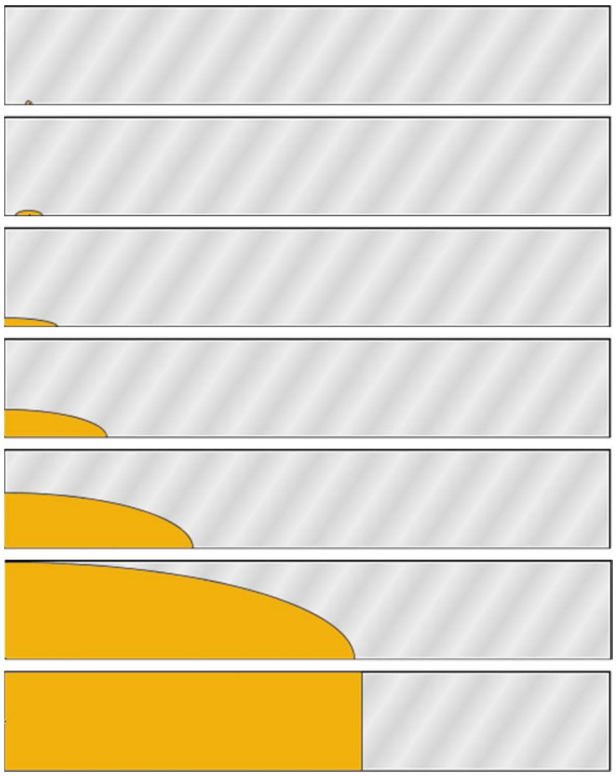

(*a*)

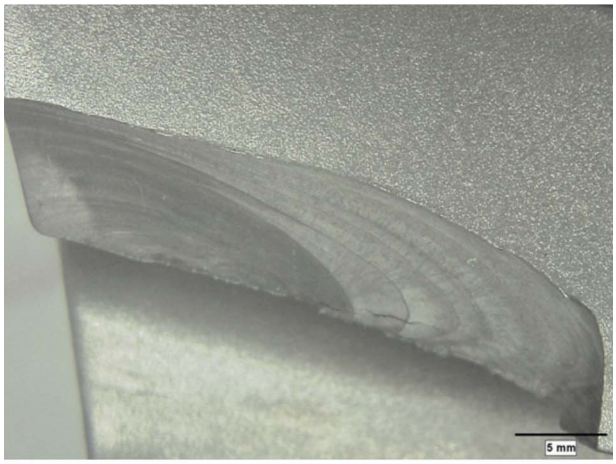


(*b*)

**Fig. 24 The crack propagation shape is dominated by the steep fretting stress gradient at the surface: (*a*) simulated crack propagation sequence and (*b*) typical failed surface**

## 6 Concluding Remarks

An approach was presented for estimating the risk reduction associated with the nondestructive inspection of aircraft engine components subjected to fretting fatigue. The approach centered on the estimation of contact stress values associated with fretting in the disk-blade interface of a typical gas turbine engine. Initial fracture risk results suggest that scheduled depot inspections have the potential to significantly reduce the probability of fracture associated with fretting fatigue for the range of values considered under this study. Further investigation is required to assess the influences of additional factors such as residual stress values and dynamic load.



Downloaded 02 Jun 2010 to 171.66.16.96. Redistribution subject to ASME license or copyright; see http://www.asme.org/terms/Terms_Use.cfm

## Acknowledgment

This work was supported by NAVAIR under Agreement No. EDO-08-SA-0021. The authors wish to acknowledge Dr. Sam Naboulsi for performing the fine mesh finite element computations at the Air Force Research Laboratory/Major Shared Resource Center (AFRL/MSRC) at Wright-Patterson AFB.

## Nomenclature

$a$ = crack depth
$a^*$ = smallest observed crack area
$c$ = half surface crack length
$E$ = Young's modulus
$F_{\text{blade}}$ = radial force of the blade acting on the disk slot
$K$ = stress intensity factor
$M$ = contact moment per unit thickness
$N_c$ = number of engines with premature cracks
$N_t$ = total number of engines in the fleet
$p$ = contact pressure traction
$P$ = normal contact force per unit thickness
$P_c$ = probability of cracking
$q$ = contact shear traction
$Q$ = shear contact force per unit thickness
$S$ = bulk stress
$t$ = thickness of disk slice
$x_0$ = center of contact
$\alpha$ = slope of shear force versus normal force in partial slip
$\zeta_a$ = crack area coefficient of variation
$\lambda_a$ = crack area median
$\Phi(\ )$ = standard normal distribution function
$\mu$ = coefficient of friction
$\Omega$ = fan rotor speed
$\theta$ = flank angle of the dovetail
$\sigma_{ij}$ = components of stress
$\Delta K_{\text{th}}$ = large-crack growth threshold
$\sigma_{xx}$ = crack opening stress
$\nu$ = Poisson's ratio

## References

[1] Frost, N. E., Marsh, K. J., and Pook, L. P., 1974, *Metal Fatigue*, Oxford University Press, Oxford, UK.
[2] Rayaproula, D., and Cook, R., 1992, "A Critical Review of Fretting-Fatigue Investigations at the Royal Aerospace Establishment," *Standardization of Fretting-Fatigue Test Methods and Equipment, ASTM STP 1159*, M. Delmi and R. Waterhouse, eds., American Society for Testing and Materials, Philadelphia, PA, pp. 129–152.
[3] Waterhouse, R., 1992, "Fretting Fatigue," Int. Mater. Rev., **37**, pp. 77–97.
[4] Lindley, T. C., 1997, "Fretting Fatigue in Engineering Alloys," Int. J. Fatigue, **19**, pp. S39–S49.
[5] Antoniou, R. A., and Radtke, T. C., 1997, "Mechanisms of Fretting-Fatigue of Titanium Alloys," Mater. Sci. Eng., A, **237**, pp. 229–240.
[6] Nicholas, T., 1999, "Critical Issues in High Cycle Fatigue," Int. J. Fatigue, **21**, pp. S221–S231.
[7] Waterhouse, R. B., 1981, "Avoidance of Fretting Fatigue Failures," *Fretting Fatigue*, R. B. Waterhouse, ed., Applied Science, London, pp. 221–240.
[8] Szolwinski, M. P., and Farris, T. N., 1996, "Mechanics of Fretting Fatigue Crack Formation," Wear, **198**, pp. 93–107.
[9] Hills, D. A., and Nowell, D., 1994, *Mechanics of Fretting Fatigue*, Kluwer, Dordrecht.
[10] Cowles, B. A., 1996, "High Cycle Fatigue in Aircraft Gas Turbines—An Industry Perspective," Int. J. Fract., **80**, pp. 147–163.
[11] Nicholas, T., and Zuiker, J. R., 1996, "On the Use of the Goodman Diagram for High Cycle Fatigue Design," Int. J. Fract., **80**, pp. 219–235.
[12] Nix, K., and Lindley, T., 1985, "The Application of Fracture Mechanics to Fretting Fatigue," Fatigue Fract. Eng. Mater. Struct., **8**, pp. 143–160.
[13] Faanes, S., and Fernando, U., 1994, "Life Prediction in Fretting Fatigue Using Fracture Mechanics," *Fretting Fatigue*, Mechanical Engineering Publications, London, UK, pp. 149–159.
[14] Conner, B. P., Lindley, T. C., Nicholas, T., and Suresh, S., 2004, "Application of a Fracture Mechanics Based Life Prediction Method for Contact Fatigue," Int. J. Fatigue, **26**, pp. 511–520.
[15] Ciavarella, M., 2003, "A 'Crack-Like' Notch Analogy for Safe-Life Fretting Fatigue Design Methodology," Fatigue Fract. Eng. Mater. Struct., **26**, pp. 1159–1170.
[16] Navarro, C., Munoz, S., and Dominguez, J., 2006, "Propagation in Fretting Fatigue From a Surface Defect," Tribol. Int., **39**, pp. 1149–1157.
[17] Chan, K. S., Lee, Y.-D., Davidson, D. L., and Hudak, S. J., 2001, "A Fracture Mechanics Approach to High Cycle Fretting Fatigue Base on the Worst Case Fret Concept," Int. J. Fract., **112**, pp. 331–353.
[18] Dini, D., Nowell, D., and Dyson, I. N., 2006, "The Use of Notch and Short Crack Approaches to Fretting Fatigue Threshold Prediction: Theory and Experimental Validation," Tribol. Int., **39**, pp. 1158–1165.
[19] Nowell, D., and Araujo, J. A., 1999, "Small Crack Methodologies and Crack Arrest in Fretting Fatigue," *Small Fatigue Cracks: Mechanics, Mechanisms, and Applications*, K. S. Ravichandran, R. O. Ritchie, and Y. Murakami, eds., Elsevier Science, Oxford, UK, pp. 361–372.
[20] Federal Aviation Administration, 2001, "Advisory Circular—Damage Tolerance for High Energy Turbine Engine Rotors," Paper No. AC 33.14-1.
[21] Federal Aviation Administration, 2008, "Advisory Circular—Damage Tolerance of Hole Features in High-Energy Turbine Engine Rotors," Paper No. AC 33.70-X.
[22] Enright, M. P., McClung, R. C., Hudak, S. J., and Francis, W. L., 2006, "Probabilistic Treatment of Crack Formation and Growth for Gas Turbine Engine Materials," ASME Paper No. GT2006-90813.
[23] Zhang, R., and Mahadevan, S., 2000, "Probabilistic Prediction of Fretting Fatigue Crack Nucleation Life of Riveted Lap Joints," *Proceedings of the 41st AIAA Structures, Dynamics, and Materials Conference*, Atlanta, GA, Apr. 3–6, Paper No. AIAA-2000-1645.
[24] Wu, Y. T., Enright, M. P., and Millwater, H. R., 2002, "Probabilistic Methods for Design Assessment of Reliability With Inspection," AIAA J., **40**(5), pp. 937–946.
[25] Golden, P. J., and Calcaterra, J., 2006, "A Fracture Mechanics Life Prediction Methodology Applied to Dovetail Fretting," Tribol. Int., **39**, pp. 1172–1180.
[26] Calcaterra, J., and Naboulsi, S., 2005, "Design Methodology to Investigate Contact Fatigue Damage in Turbine Engine Hardware," Int. J. Fatigue, **27**, pp. 1133–1141.
[27] Gean, M. C., and Farris, T. N., 2005, "Finite Element Analysis of the Mechanics of Blade/Disk Contacts," *Proceedings of the 46th AIAA Structures, Structural Dynamics, and Materials Conference*, Austin, TX, Apr. 18–21.
[28] Golden, P. J., 2009, "Development of a Dovetail Fretting Fatigue Fixture for Turbine Engine Materials," Int. J. Fatigue, **31**, pp. 620–628.
[29] McVeigh, P. A., Harish, G., Farris, T. N., and Szolwinski, M. P., 1999, "Modeling Interfacial Conditions in Nominally Flat Contacts for Application to Fretting Fatigue of Turbine Engine Components," Int. J. Fatigue, **21**, pp. S157–S165.
[30] Chan, K. S., Lee, Y.-D., Davidson, D. L., and Hudak, S. J., 2001, "A Fracture Mechanics Approach to High Cycle Fretting Fatigue Base on the Worst Case Fret Concept," Int. J. Fract., **112**, pp. 299–330.
[31] Ciavarella, M., Hills, D. A., and Monno, G., 1998, "The Influence of Rounded Edges on Indentation by a Flat Punch," Proc. Inst. Mech. Eng., Part C: J. Mech. Eng. Sci., **212**, pp. 319–328.
[32] Simulia, 2007, ABAQUS Documentation, Providence, RI.
[33] Southwest Research Institute, 2008, "DARWIN® User's Guide," San Antonio, TX.



Downloaded 02 Jun 2010 to 171.66.16.96. Redistribution subject to ASME license or copyright; see http://www.asme.org/terms/Terms_Use.cfm